PERGAMON

International Journal of Solids and Structures 38 (2001) 7899–7918

INTERNATIONAL JOURNAL OF SOLIDS and STRUCTURES

www.elsevier.com/locate/ijsolstr

Modeling the interaction between densification mechanisms in powder compaction

S.J. Subramanian, P. Sofronis *

Department of Theoretical and Applied Mechanics, University of Illinois at Urbana-Champaign, 216 Talbot Laboratory, 104 South Wright Street, Urbana IL 61801, USA

Received 24 July 2000; in revised form 18 April 2001

Abstract

In this paper a micromechanical model of the interaction between densification mechanisms in powder compaction is presented. It accounts for elastic and power-law creep deformation of the bulk material along with stress-driven diffusion along the interparticle contact areas and curvature-driven diffusion on the pore surfaces. The finite element method is used to obtain the time-dependent deformation of the powder aggregate under plane strain deformation conditions. To reduce the number of case calculations needed to analyze the process, important dimensionless parameters that measure the relative magnitude of the densification mechanisms are identified. The calculated densification rates of the compact are compared with those predicted by analytical models, and conclusions are drawn on the significance of including the interaction between the densifying mechanisms in powder compaction models.

Keywords: Creep; Compaction; Contact; Diffusion; Finite element; Micromechanics

1. Introduction

In powder densification the closing of porosity typically occurs by various deformation mechanisms such as linear elasticity, rate-independent plasticity, power-law creep, diffusion along the interparticle contacts and pore surfaces, and interparticle slip (Ashby, 1974; Swinkels and Ashby, 1981; Helle et al., 1985).

Models for the early stages of densification (when the porosity is interconnected) have been proposed in which the single dominant mechanism is plasticity (Fleck et al., 1992; Akisanya et al., 1994; Akisanya and Cocks, 1995; Fleck, 1995), power-law creep (Ashby, 1974; Swinkels and Ashby, 1981; Kuhn and McMeeking, 1992; Bouvard, 1993; Storakers, 1997; Larsson et al., 1996; Storakers et al., 1997; Storakers et al., 1999), interparticle diffusion (McMeeking and Kuhn, 1992) or interparticle slip (Casagranda and Sofronis, 1997). Work has also been done in the area of coupling interparticle diffusion to pore surface diffusion (Bross and Exner, 1979; Pan and Cocks, 1995; Svoboda and Riedel, 1995; Zhang and Schneibel,

* Corresponding author. Tel.: +1-217-333-2636; fax: +1-217-244-5707.
E-mail address: sofronis@uiuc.edu (P. Sofronis).

0020-7683/01/$ - see front matter
PII: S0020-7683(01)00096-8

1995; Bouvard and McMeeking, 1996; Pan et al., 1997) and linear elastic deformation to surface diffusion (Freund et al., 1993; Suo and Wang, 1994; Wang and Suo, 1997; Xia et al., 1997). An excellent overview of diffusive processes in the context of cavitation at grain interfaces can be found in the work of Chuang et al. (1979). Arzt and coworkers (Arzt, 1982; Arzt et al., 1983; Fishcmeister and Arzt, 1983) developed a model for densification that takes into account the evolving particle coordination number and contact size during densification. Subsequently, a variety of models have used their idea of isotropically evolving contact areas to predict the macroscopic behavior of a powder compact (Helle et al., 1985; McMeeking and Kuhn, 1992). Similarly, models for the final stages of densification (when the pores are isolated) are based on power-law creep (Cocks, 1989; Duva and Crow, 1992; Sofronis and McMeeking, 1992), diffusional creep (Riedel et al., 1994b, Svoboda et al., 1994) or interparticle diffusion and slip (Riedel et al., 1994a). An overview of the analytical investigations into powder compaction can be found in the work of Cocks (1994). Significantly, in this work, Cocks has considered the interaction between pairs of competing mechanisms in effecting the overall compaction of the particles.

A detailed study of the concurrent action of the densifying mechanisms is an important prerequisite for the development of densification models with predictive capabilities. In the current paper a micromechanical framework that captures the coupled action of most of the densification mechanisms is presented. In the proposed model, densification begins with the initial contact between particles established by instantaneous elastic deformation, and proceeds in time through combined elastic and power-law creep deformation in the bulk coupled with diffusional mass transport on the interparticle contact areas and pore surfaces. In order to understand the mechanics of coupling, attention is focused on the calculation of micromechanical parameters such as volumetric flux distribution along the interparticle contact areas and pore surface, and pore shape evolution during densification. The modeling of the bulk of the particles as elastic and creeping, and the monitoring of the contact evolution between particles are points of departure from some of the previous models (e.g., Bross and Exner, 1979; McMeeking and Kuhn, 1992; Svoboda and Riedel, 1995; Zhang and Schneibel, 1995; Bouvard and McMeeking, 1996) that dealt with interparticle and pore surface diffusion under the assumption of rigid particles. Another important ingredient in the present model is the enforcement of the classical Laplace relationship between the pore curvature, energy of the pore surface, and the normal stresses in the adjoining bulk material (Herring, 1951; Rice and Chuang, 1981; Freund et al., 1993).

In the numerical calculations, the problem of densification of a square array of cylinders under hydrostatic loading is considered in order to simulate hot isostatic pressing (HIPing). Pure HIPing was considered solely to reduce the degree of numerical complexity that would arise from interparticle slip if the applied macroscopic stress had a non-zero deviatoric component. A small-displacement formulation is used to describe the deformation of the compact. Of course, the validity of such an approach is limited to small geometry changes of the aggregate. Thus, a finite element formulation with no nodal updating is developed and implemented in a unit cell to solve the relevant initial boundary value problem under plane strain conditions. The proposed numerical scheme is marched in time in order to capture the evolution of the densification process. It should be emphasized that the formulation developed in this work is equally valid for general loading states, though an appropriate unit cell has to be chosen to accommodate the applied stresses and suitable modifications to the governing equations have to be made to account for interparticle slip (Needleman and Rice, 1980; Casagranda and Sofronis, 1997).

2. Material constitutive laws

The total strain rate is defined through the velocity as $\dot{\varepsilon}_{ij} = (v_{i,j} + v_{j,i})/2$, where $(\cdot)_{,j} = \partial(\cdot)/\partial x_j$ and the superposed dot denotes differentiation with respect to time, and is decomposed into an elastic component

$\dot{\varepsilon}^{\mathrm{e}}_{ij}$ and a creep component $\dot{\varepsilon}^{\mathrm{c}}_{ij}$ such that $\dot{\varepsilon}_{ij} = \dot{\varepsilon}^{\mathrm{e}}_{ij} + \dot{\varepsilon}^{\mathrm{c}}_{ij}$. The elasticity of the particle is characterized by the standard Hooke's law

$$\sigma_{ij} = C_{ijkl}\varepsilon^{\mathrm{e}}_{ij}, \tag{1}$$

where C_{ijkl} are the components of the isotropic elastic modulus tensor, and the Einstein summation convention is implied over a repeated index. The creep strain rate $\dot{\varepsilon}^{\mathrm{c}}_{ij}$, which obeys incompressibility, is given by the standard power-law creep relationship

$$\dot{\varepsilon}^{\mathrm{c}}_{ij} = 3C\sigma^{n-1}_{\mathrm{e}}s_{ij}/2, \tag{2}$$

where $\sigma_{\mathrm{e}} = \sqrt{3s_{ij}s_{ij}/2}$ is the effective stress, $s_{ij} = \sigma_{ij} - (\sigma_{kk}/3)\delta_{ij}$ is the deviatoric stress, n is the creep exponent, $C \equiv \dot{\varepsilon}_0/\sigma^n_0$ is the creep modulus, $\dot{\varepsilon}_0$ and σ_0 are material parameters in the uniaxial tension relation $\dot{\varepsilon}/\dot{\varepsilon}_0 = (\sigma/\sigma_0)^n$, and δ_{ij} is the Kronecker delta.

Diffusion along the interparticle contact areas or the pore surface is driven by chemical potential gradients (Herring, 1951) such that

$$j_{\mathrm{b}} = \mathscr{D}_{\mathrm{b}}\,\mathrm{d}\sigma_{\mathrm{n}}/\mathrm{d}s \tag{3}$$

along the interparticle area, and

$$j_{\mathrm{p}} = \mathscr{D}_{\mathrm{p}}\,\mathrm{d}(\gamma_{\mathrm{p}}k)/\,\mathrm{d}s \tag{4}$$

along the pore surface. Here, j_{b} and j_{p} are the volumetric fluxes per unit length along a direction s tangential to the interparticle and the pore surface areas respectively (see Fig. 1a and b), $\mathscr{D}_{\mathrm{b}} = D_{\mathrm{b}}\delta_{\mathrm{b}}\Omega/KT$ and $\mathscr{D}_{\mathrm{p}} = D_{\mathrm{p}}\delta_{\mathrm{p}}\Omega/KT$ are correspondingly interparticle and pore surface diffusivities having dimensions of volume divided by stress per unit time, D_{b} and D_{p} are the corresponding diffusion coefficients, δ_{b} and δ_{p} are the corresponding effective thicknesses through which matter diffuses, σ_{n} is the stress normal to the contact area, k and γ_{p} are respectively the curvature and the energy of the pore surface (Fig. 1a and b), Ω is the atomic volume of the diffusing species, K is Boltzmann's constant, and T is the absolute temperature.

In order to describe matter conservation, let $\dot{h}(s)$ be the normal overlapping rate that would have resulted had the particles been free to penetrate into one another under the action of external load. Since the particles in reality do not plough into each other, all the mass that would otherwise interpenetrate is assumed to be transported along the contact areas by interparticle diffusion. Matter conservation along the interparticle contact area requires

$$\frac{\mathrm{d}j_{\mathrm{b}}(s)}{\mathrm{d}s} + \dot{h}(s) = 0. \tag{5}$$

For the calculation of $\dot{h}(s)$, consider two points on the boundaries of particles I and II with corresponding velocities v^{I}_i and v^{II}_i (see Fig. 1a and Appendix A), i.e., v^{I}_i and v^{II}_i are the velocities of matter on each side of the interface that develops when the particles come into contact. Since the points are initially a distance $\Delta g(s)$ apart (Fig. 1a), the normal overlapping rate $\dot{h}(s)$ is expressed as

$$\dot{h}(s) = \left(v^{\mathrm{I}}_i(s) - v^{\mathrm{II}}_i(s)\right)n_i + \dot{g}(s) = v_{\mathrm{n}}(s) + \dot{g}(s), \tag{6}$$

where $v_{\mathrm{n}}(s)$ is the relative normal velocity of approach, n_i are the components of the unit normal to the contact area (see Fig. 1a), and $\dot{g}$ is the rate of change of the gap Δg. In other words, the entire relative normal velocity does not contribute to the mass flux when these two points come into contact; part of it goes toward bridging the gap. Of course, for points that are already in contact, $\Delta g = 0$, $\dot{g} = 0$, $\dot{h}(s) = v_{\mathrm{n}}(s)$, and thus the entire relative normal velocity v_{n} results in a change of the volumetric flux. In this case, one recovers the form of the matter conservation equation employed by Needleman and Rice (1980) in their study of diffusive cavitation along grain boundaries.

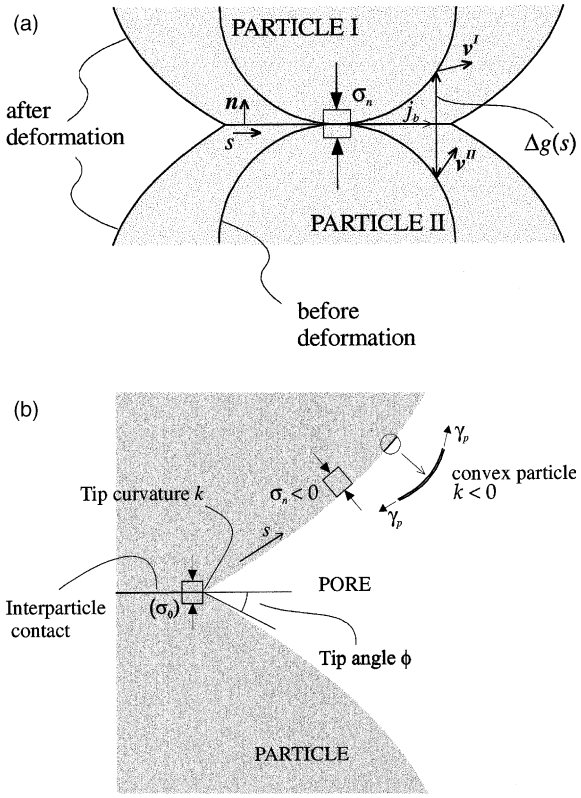

Fig. 1. (a) The interparticle contact area: s is the arclength, **n** is the unit normal vector, σ_{n} is the normal stress, j_{b} is the volumetric flux and $\Delta g(s)$ is the non-negative gap function. (b) Sign convention for curvature on the pore surface: k is negative if the center of curvature is in the region occupied by the particle (pore is concave) and correspondingly the stress is compressive.

Along the pore surface, matter conservation dictates that

$$\frac{\mathrm{d}j_{\mathrm{p}}(s)}{\mathrm{d}s} + \dot{\alpha}(s) = 0, \tag{7}$$

where $\dot{\alpha}(s)$ is the local particle expansion rate (Fig. 2), measured normal to the particle surface, and is positive when matter is deposited on the pore surface and negative when the pore surface is eroded. Here it should be emphasized that though the rate $\dot{\alpha}$ relates to the flux on the pore surface just as the normal relative velocity v_{n} does to the flux on the interparticle contact areas, $\dot{\alpha}$ is not the velocity of any material point on the pore surface; it is simply the rate at which mass is added to or removed from the pore surface.

Equilibrium at any arbitrary point on the pore surface is described by the standard Laplace equation (Gurtin and Murdoch, 1975; Rice and Chuang, 1981; Freund et al., 1993) that relates the normal stress σ_{n} in the adjoining bulk material to the local curvature k

$$\sigma_{\mathrm{n}}(s) = \gamma_{\mathrm{p}} k(s). \tag{8}$$

In the present model, surface tension γ_{p} is assumed to be constant and therefore, the tangential stress on the pore surface is zero (Rice and Chuang, 1981; Freund et al., 1993). The sign conventions for curvature and

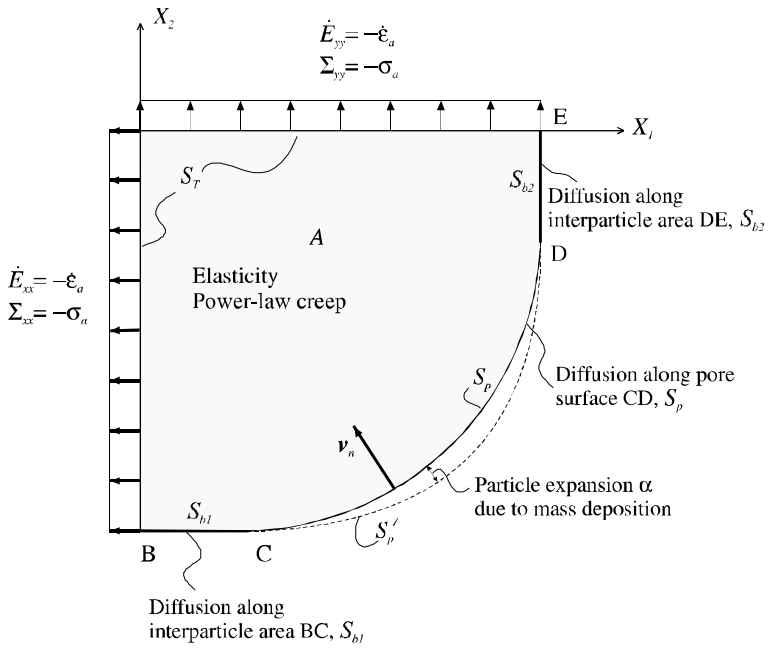

Fig. 2. Definition of the domain and boundary conditions for the unit cell.

normal stress are shown in Fig. 1b. At the junction between the interparticle contact area and the pore surfaces (tip), both volumetric flux and chemical potential are continuous. Chemical potential continuity requires that

$$\sigma_0 = \gamma_p k_0, \tag{9}$$

where the subscript 0 is used to denote values of σ_n and k at the junction.

3. The unit cell model

Due to the symmetry of the square particle arrangement, the densification is studied by considering the deformation of just one quadrant of the cylinder as shown in Fig. 2. (Though it is sufficient to consider one-eighth of the circle for the present loading case, the current unit cell has been chosen in order to accommodate the more general case of unequal applied principal loads.) This particular choice has been made in view of the fact that the unit normals to the contact areas are known a priori. This offers a significant simplification with respect to the numerical evaluation of the contact areas and reduces the number of iterations and computation time considerably. The study of the densification process is carried out by considering the following two coupled problems concurrently (Fig. 2): (i) the *bulk deformation of the particle* that also involves the interparticle contact area evolution along with interparticle diffusion, and the effect of the pore surface stress induced by the curvature; and (ii) the *pore surface diffusion* for the calculation of the particle expansion $\alpha(s)$ along the pore surface.

3.1. Deformation of the particle

Extending the formulation of Needleman and Rice (1980) to include the effects of stress induced by pore surface curvature, one can state the principle of virtual power for the deformation of the particle (Fig. 2) in the following form:

$$\int_{S_T} T_i\,\delta v_i\,\mathrm{d}s = \int_{\mathrm{A}} \sigma_{ij}\,\delta\dot{\varepsilon}_{ij}\,\mathrm{d}A + \int_{S_\mathrm{b}} \sigma_\mathrm{n}\,\delta\dot{h}\,\mathrm{d}s + \int_{S_\mathrm{p}} \sigma_\mathrm{n}\,\delta v_\mathrm{n}\,\mathrm{d}s + \gamma_\mathrm{b}\,\delta\dot{a}_1 - \gamma_\mathrm{p}(\delta v_\mathrm{tip}\cos\phi)_\mathrm{C} + \gamma_\mathrm{b}\,\delta\dot{a}_2 - \gamma_\mathrm{p}(\delta v_\mathrm{tip}\cos\phi)_\mathrm{D}. \tag{10}$$

Here T_i is specified traction on the external boundary S_T of the unit cell, σ_{ij} are the stress components within the bulk region A occupied by the particle, δv_i is an arbitrary virtual variation of the velocity on S_T and in A, $\delta\dot{\varepsilon}_{ij}$ is the corresponding strain rate variation, σ_n is the normal stress either on the interparticle area $S_\mathrm{b} = S_{\mathrm{b}1} \cup S_{\mathrm{b}2}$ or the pore surface area S_p (that is the boundary S–S_T–S_b of the particle deforming by elasticity and creep before the deposition of the mass transported by surface diffusion, (Fig. 2)), δv_n is the virtual variation of the normal velocity of points on the pore surface S_p, $\delta\dot{h}$ is the virtual rate of $\dot{h}$ along contact area $S_\mathrm{b} = S_{\mathrm{b}1} \cup S_{\mathrm{b}2}$ such that $\delta\dot{h} = \delta v_\mathrm{n} + \delta\dot{g} = \delta v_\mathrm{n}$ (see Eq. (6)) since the gap $\Delta g(s)$ is a fixed part of the particle geometry at any instant of time, and ϕ_C and ϕ_D are the dihedral angles at (tip) points C and D and are shown schematically as angle ϕ in Fig. 1b. The parameters $\delta\dot{a}_1$ and $\delta\dot{a}_2$ are respectively virtual rates of change of the two contact areas $S_{\mathrm{b}1}$ and $S_{\mathrm{b}2}$ (equal in the present isostatic simulations), and δv_tip is the virtual relative velocity at the junctions C and D (Fig. 2) tangential to the contact areas, measured positive if it causes an increase in the area of contact. The algebraic terms in Eq. (10) involving γ_b and γ_p represent the power expended/released as the densification proceeds and matter having energy γ_b on the interparticle areas acquires energy γ_p when deposited on the pore surface. Though the pore surface could change its length due to tangential stretching, there is no virtual power term associated with this mode of deformation since the stress tangential to the surface is zero owing to the assumption that the surface tension is constant over the entire pore surface. In accordance with the definition of S_p, the mass deposited on S_p by free surface diffusion (i.e., the mass in the area bounded by S_p and the pore free surface S'_p as shown in Fig. 2) is not considered as part of the particle bulk area A, and as such, it is not accounted for in the first integral on the right hand side of Eq. (10). This approximation is consistent with the small displacement assumption in the model, that is, the analysis is valid for small relative density changes. However, in view of the marked effect this accumulated mass has on the pore surface curvature, the normal stress σ_n along S_p (in the third integral of the right hand side of Eq. (10)) is related through Eq. (8) to the curvature of the pore free surface S'_p as is configured by the deposited mass and continuously changes with time. As a result, the calculation of σ_n along S_p depends on both the particle deformation and the particle expansion α, and this couples the problem (i) for the deformation of the particle to the problem (ii) for the pore surface diffusion.

Starting with Eq. (3) and using the divergence theorem, one can cast the second integral over the area $S_\mathrm{b} = S_{\mathrm{b}1} \cup S_{\mathrm{b}2}$ on the right hand side of Eq. (10) into

$$\int_{S_\mathrm{b}} \sigma_\mathrm{n}\,\delta\dot{h}\,\mathrm{d}s = \int_{S_\mathrm{b}} \frac{1}{\mathscr{D}_\mathrm{b}} j_\mathrm{b}\,\delta j_\mathrm{b}\,\mathrm{d}s + (\sigma_0\,\delta j_\mathrm{b})_\mathrm{D} - (\sigma_0\,\delta j_\mathrm{b})_\mathrm{C}, \tag{11}$$

where δj_b and $\delta\dot{h}$ are virtual fields that satisfy the zero flux condition at points B and E and are related by $\mathrm{d}\delta j_\mathrm{b}/\mathrm{d}s + \delta\dot{h} = 0$. Upon substitution of Eqs. (8) and (11) into Eq. (10), one obtains

$$\int_S T_i\,\delta v_i\,\mathrm{d}s = \int_{\mathrm{A}} \sigma_{ij}\,\delta\dot{\varepsilon}_{ij}\,\mathrm{d}A + \int_{S_\mathrm{p}} \gamma_\mathrm{p} k\,\delta v_\mathrm{n}\,\mathrm{d}s + \int_{S_\mathrm{b}} \frac{1}{\mathscr{D}_\mathrm{b}} j_\mathrm{b}\,\delta j_\mathrm{b}\,\mathrm{d}s + (\sigma_0\,\delta j_\mathrm{b})_\mathrm{D} - (\sigma_0\,\delta j_\mathrm{b})_\mathrm{C} + \gamma_\mathrm{b}\,\delta\dot{a}_1 - \gamma_\mathrm{p}(\delta v_\mathrm{tip}\cos\phi)_\mathrm{C} + \gamma_\mathrm{b}\,\delta\dot{a}_2 - \gamma_\mathrm{p}(\delta v_\mathrm{tip}\cos\phi)_\mathrm{D}. \tag{12}$$

By appropriate interpolations, Eq. (12) is converted into a set of non-linear finite element equations (Eq. (A.5), Appendix A). The contact areas BC and DE (Fig. 2), which are domains for the interparticle diffusion process, are not known beforehand and are determined as part of the solution. The overall solution strategy is incremental in time and involves assuming a size for the contact areas that is in excess of the expected. By a Newton iteration scheme (''global loop''), the finite element Eq. (A.5) are satisfied at time $t_{n+1} = t_n + \Delta t$ by solving for displacement increments $\{\Delta u\}$ using the known stresses $\{\sigma\}_n$ and displacements $\{u\}_n$ at time t_n. Then, the contact areas are checked for consistency, i.e., whether nodes assumed to be diffusive are indeed in contact. If this condition is not met, the assumed size of the contact areas is reduced by a node and the procedure is repeated until the solution is consistent. In setting up the finite element equations (A.5) for the displacement increments, the creep strain increment portion of the total strain increment associated with an assumed displacement increment is unknown. Thus, for such an assumed displacement increment, a creep strain increment is calculated at each integration station by integrating the combined elastic, power-law creep constitutive equations through the trapezoidal rule and by using the Newton iteration method to solve the resulting set of four algebraic equations (''local loop''). These two iterative schemes, global and local, continue till convergent increments of displacement and creep strain are obtained, of course, for the assumed contact areas BC and DE. The creep strain rate and displacement increments at time t_n are used to initiate the process.

3.2. The pore surface diffusion problem for the calculation of the expansion $\alpha(s)$

Solution to the problem (i) yields the volumetric flux j_C and j_D respectively at $s = s_C$ and $s = s_D$ (see Fig. 2) at time t_{n+1} and the coordinates $\{X\}_{n+1} = \{X\}_n + \{\Delta u\}$ of the nodes on the pore surface S_p. These pieces of information are used to integrate Eqs. (4) and (7) to obtain the expansion increments $\{\Delta\alpha\}$ at time t_{n+1} such that $\{\alpha\}_{n+1} = \{\alpha\}_n + \{\Delta\alpha\}$ and surface S'_p is determined from $\{X\}_{n+1} + \{\alpha\}_{n+1}$ (Appendix B).

In summary, the solution to problem (i) enforces equilibrium in the bulk of the particle, ensures the satisfaction of the diffusion equation (3) on the interparticle boundaries BC and DE, and of the Laplace relation (8) on the pore surface S_p. The solution to problem (ii) ensures mass conservation on the pore surface as dictated by Eq. (7), as well as enforcement of the pore surface diffusion equation (4) and chemical potential continuity at the tips C and D (Eq. (9)).

4. Dimensionless groups

Dimensional analysis over the geometric, material, and loading parameters leads to the following dimensionless groups:

$$\psi_b = \frac{\gamma_b}{\sigma_a R}, \quad \psi_p = \frac{\gamma_p}{\sigma_a R}, \quad \chi_b = \frac{\mathscr{D}_b}{C\sigma_a^{n-1} a_0^2 R}, \quad \chi_p = \frac{\mathscr{D}_p \gamma_p}{C\sigma_a^n R^4} \tag{13}$$

where R is the particle radius, a_0 is the size of the instantaneous elastic contact (Raj, 1974) at $t = 0$, and σ_a is the applied macroscopic stress (Fig. 2).

Clearly, ψ_b and ψ_p represent the strengths of the interface and pore surface tension in relation to the applied stress. The higher these values are, the larger is the energy required to be delivered by the applied loads to change the respective areas of these surfaces. Also for a given pore curvature, a higher value of ψ_p implies higher normal stresses in the adjoining bulk material.

Groups χ_b and χ_p can also be arrived at by considering the magnitudes of typical strain rates that are representative of the three densification processes, namely power-law creep deformation in the bulk, interparticle diffusion, and pore surface diffusion. A measure of the creep strain rate is readily expressed in terms of the creep modulus and the applied stress through $\dot{\varepsilon}^c = C\sigma_a^n$. From Eq. (3), $j_b \propto \mathscr{D}_b \sigma_a / a_0$, which

along with Eq. (5) yields $\dot{h} \propto \mathscr{D}_b \sigma_a / a_0^2$. Then a measure of the strain rate due to interparticle diffusion can be calculated as $\dot{\varepsilon}^b \propto \dot{h}/R = \mathscr{D}_b \sigma_a / a_0^2 R$. Similarly, a measure of the strain rate due to pore surface diffusion can be expressed as $\dot{\varepsilon}^p \propto \mathscr{D}_p \gamma_p / R^4$. Then, one readily sees that $\chi_b = \dot{\varepsilon}_b / \dot{\varepsilon}_c$ and $\chi_p = \dot{\varepsilon}_p / \dot{\varepsilon}_c$. Thus, χ_b and χ_p measure respectively the densification strength of the interparticle and surface diffusion processes relative to the power-law creep process in the bulk. For example, if $\chi_b = 10$ and $\chi_p = 100$, one can infer that the interparticle and pore surface diffusion processes are respectively one and two orders of magnitude faster than the power-law creep process.

Characteristic time scales for each of the three rate mechanisms can be defined by considering the time required for each process to yield a strain equal to a reference strain, which is chosen as the elastic strain σ_a/E (where E is the Young's modulus) corresponding to the applied stress σ_a. Thus, the following characteristic times can be defined respectively for power-law creep, interparticle diffusion and pore surface diffusion

$$t_c = \frac{\varepsilon^e}{\dot{\varepsilon}^c} = \frac{\sigma_a/E}{C\sigma_a^n} = \frac{1}{EC\sigma_a^{n-1}}, \quad t_b = \frac{\varepsilon^e}{\dot{\varepsilon}_b} = \frac{a_0^2 R}{\mathscr{D}_b E}, \quad t_p = \frac{\varepsilon^e}{\dot{\varepsilon}_p} = \frac{R^4 \sigma_a}{\mathscr{D}_p E \gamma_p}. \tag{14}$$

5. Numerical results

A notable feature of the present formulation is that if the interparticle diffusion coefficient is assumed to have a very small value, the free surface diffusion coefficient is set equal to zero, and the effects associated with γ_b and γ_p are neglected, it is equivalent to a penalty method treatment for the solution of the contact problem. This feature was employed to calculate the elastic solution at time $t = 0$, which serves as the starting point for the subsequent time-dependent deformation of the unit cell. In order to validate this penalty method, the problem of contact between two spheres deforming by pure power-law creep (elasticity and diffusion processes were switched off) was studied under axisymmetric deformation (see inset of Fig. 3). The finite element results for creep exponent $n = 3$ were compared with those of Storakers et al. (1999) who investigated the viscoplastic contact between two spheres. Storakers et al. (1999) described the time-dependent contact evolution through two scaling laws, which in the case of pure creep specialize to $F = Q(n) h^{1-1/2n} \dot{h}^{1/n}$ and $a^2 = hRc^2$, where F is the applied force, h is the distance of approach of the centers of the two spheres and $\dot{h}$ its time rate of change, a is the radius of the contact zone, R is the undeformed radius of the sphere (see inset of Fig. 3), $Q(n) = \pi(1 + 2/n)2^{-2/n}3^{1-2/n}C^{-1/n}c^{2+1/n}R^{1-1/2n}$, and $c^2 = 1.43e^{-0.97/n}$. Fig. 3 illustrates the comparison between the finite element results of the present study as a function of a and those obtained by Storakers et al. (1999). Clearly, the present finite element code reproduces the results of Storakers et al. (1999) fairly accurately.

For times $t > 0$, the solution to the unit cell problem (problems (i) and (ii)) was obtained by the procedure outlined in Section 3 and macroscopic quantities such as density and densification rate were calculated. Eight-noded isoparametric elements were used with a 2×2 rule for integration of the stiffness matrices. The incompressibility of the creep deformation was enforced by the method of Nagtegaal et al. (1974). The mesh used in the calculation had 920 elements and 2481 nodes, out of which 321 nodes were sequentially numbered and placed along the arc BCDE to discretize the contact areas and the pore surface.

The undeformed particle radius was $R = 1$ and this corresponds to an initial area fraction of particles of 0.785. With $\chi_b = 5000$, $\psi_p = 0.01$, $\psi_b = 0.003$, $\sigma_a/E = 0.001$, Poisson's ratio $v = 0.33$, and creep exponent $n = 5$, finite element results were obtained for $\chi_p = 20$ and 10^8 (very slow and very fast pore surface diffusion as will be discussed below). The applied macroscopic stress state was $\Sigma_{xx} = \Sigma_{yy} = -\sigma_a$ as shown in Fig. 2. The initial marching time step was $\Delta t = 5 \times 10^{-5} t_b$, and as the powder aggregate relaxed and densified, the magnitude of the time step was progressively increased. Calculations were carried out till the

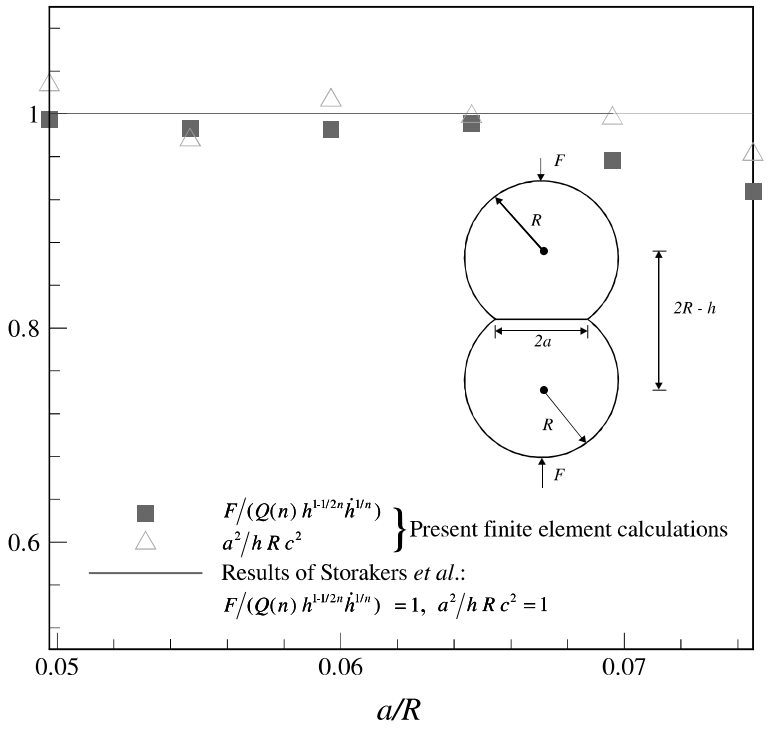

Fig. 3. Contact between two spheres deforming only by power-law creep. Creep exponent $n = 3$, $Q(n) = \pi(1 + 2/n)2^{-2/n}3^{1-2/n} \times C^{-1/n}c^{2+1/n}R^{1-1/2n}$, and $c^2 = 1.43e^{-0.97/n}$.

total elapsed time was equal to $t = 60t_b$. At this stage, nodal displacements were observed to be quite large and the present small-displacement scheme with no nodal updating was deemed to be inadequate and hence, no further computations were carried out. Using Eqs. (13) and (14), one can estimate $\varepsilon^e/\varepsilon^c = t_c/t = \chi_b t_b/t$. Since $\chi_b = 5000$ and the largest value of t/t_b is 60, it is to be expected that during the entire range of deformation considered, the magnitude of the creep strains is small when compared to the elastic strains. Indeed, even at $t/t_b = 60$, the calculated creep strains were negligible in comparison to the total strains at the integration stations.

For the case $\chi_p = 20$, the deformed outline of the unit cell at different time instants is shown in Fig. 4. The interparticle contact areas increase progressively with time and as the particle densifies and the pore closes, the particle shape is clearly non-circular. In contrast, calculations with $\chi_p = 10^8$ showed that the particle always maintains its circular shape, suggesting that $\chi_p = 10^8$ represents extremely fast surface diffusion. Attention should be drawn to the fact that the observed particle shape evolution results from the action of the interparticle stress gradients and the resulting mass flow toward the pore surface. These gradients are set by the interaction between the particle deformation and the diffusive relaxation along contact areas and pore surface.

Figs. 5 and 6 show the flux profiles on the interparticle contacts and pore surface as functions of the arc length s at various values of the normalized time t/t_b for $\chi_p = 20$ and 10^8 respectively. Note that $s = 0$ at point B, $s = s_{max}$ at point E (Fig. 2), and the flux is normalized by a reference value $j_{ref} = \mathscr{D}_b\sigma_a/s_{max}$. At the earlier stages, the flux gradient at point C and in its neighborhood on S_p is positive (negative at D) due to the fact that $\mathscr{D}_p\,dk/ds$ is greater (less) than $\mathscr{D}_b\,d\sigma_n/ds$ at C (D). As the contact areas increase, this trend is reversed at the later stages since the demand for mass by the pore surface decreases. As a result, the peaks in

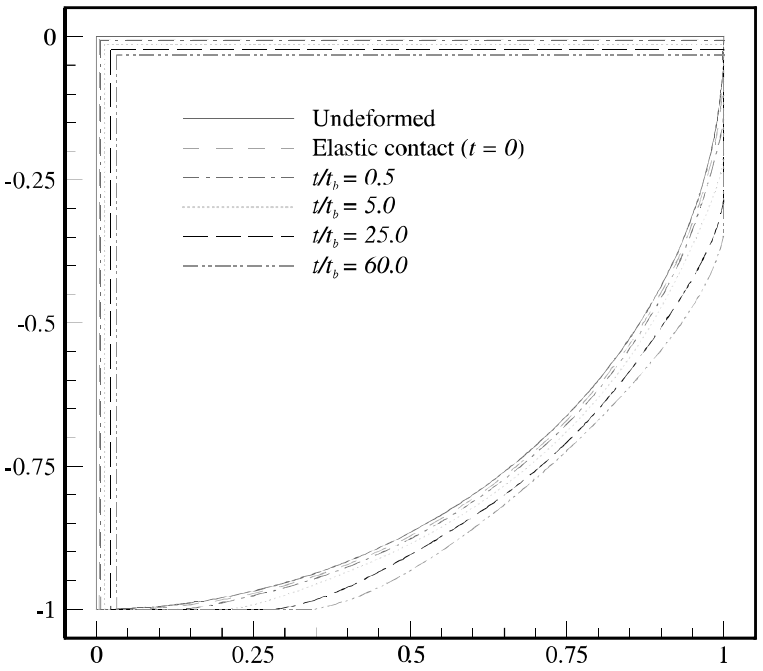

Fig. 4. Deformed outline of the unit cell when pore surface diffusion is slow: $\chi_b = 5000$, $\chi_p = 20$, $\psi_p = 0.01$, $\psi_b = 0.003$, $\sigma_a/E = 0.001$, $n = 5$ and $v = 0.33$.

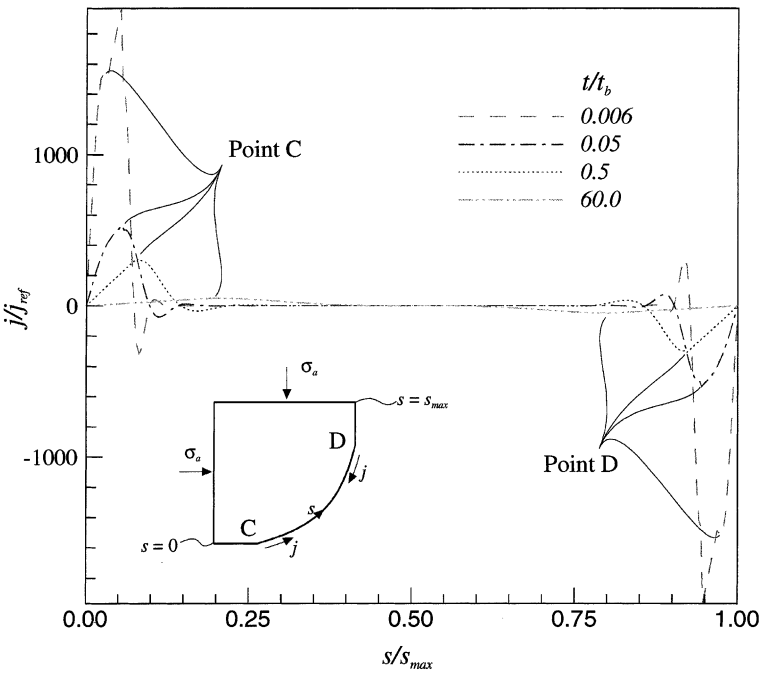

Fig. 5. Flux on the interparticle contact areas and pore surface when pore surface diffusion is slow: $\chi_b = 5000$, $\chi_p = 20$, $\psi_p = 0.01$, $\psi_b = 0.003$, $\sigma_a/E = 0.001$, $n = 5$, and $v = 0.33$. Notice that $j = j_b$ on S_b, $j = j_p$ on S_p, and $j_{ref} = \mathscr{D}_b\sigma_a/s_{max}$.

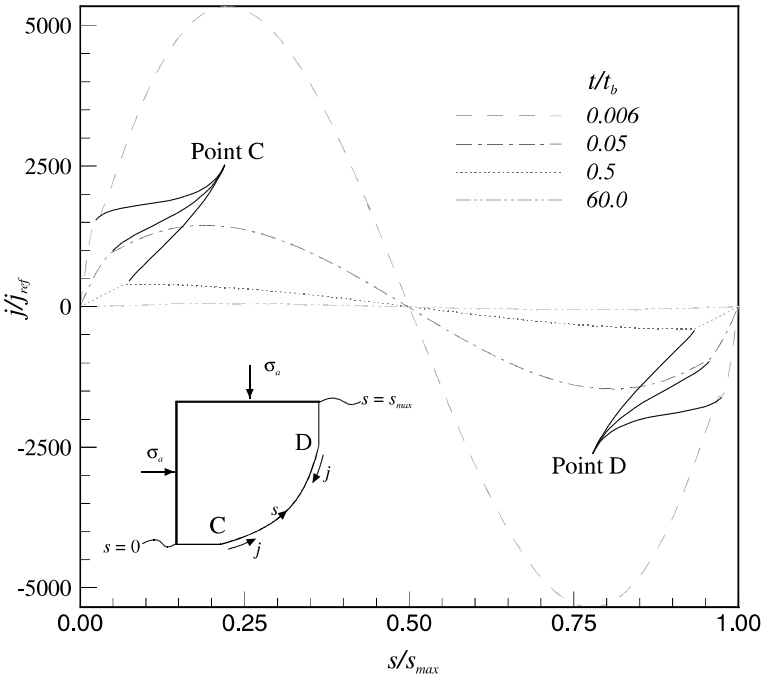

Fig. 6. Flux on the interparticle contact areas and pore surface when pore surface diffusion is extremely fast: $\chi_b = 5000$, $\chi_p = 10^8$, $\psi_p = 0.01$, $\psi_b = 0.003$, $\sigma_a/E = 0.001$, $n = 5$, and $\nu = 0.33$. Notice that $j = j_b$ on S_b, $j = j_p$ on S_p, and $j_{ref} = \mathscr{D}_b\sigma_a/s_{max}$.

the magnitude of the volumetric flux coincide with the location of the boundaries of the interparticle areas (that is, points C and D). Note that the midpoint of the pore is a point of reflection for the flux profiles. The anti-symmetry of the flux profiles about $s = s_{max}/2$ derives from the hydrostatic compaction state, that is, equal amounts of mass diffuse out of the two contact areas BC and DE toward the pore surface. Both sets of flux profiles flatten out as time elapses, and this is again in accordance with diffusion-induced relaxation whereby the gradients in stress and curvature reduce with time, thus resulting in less amounts of volumetric diffusion. In the fast surface diffusion case ($\chi_p = 10^8$), matter transport occurs over the entire pore surface whereas in the case of $\chi_p = 20$, mass transport is restricted to regions near the tip points C and D (Fig. 2) and flux is negligible over the rest of the pore surface. This almost total inability of the pore surface diffusion to redistribute evenly the incoming flux implies that $\chi_p = 20$ represents very slow surface diffusion.

In Fig. 7, the normalized curvature $k/(1/R)$ of the pore surface is shown plotted against normalized arclength s/s_{max} at various instants of time for the slow surface diffusion case $\chi_p = 20$. As expected, a symmetric variation about the midpoint is observed and significant curvature gradients persist since slow surface diffusion cannot neutralize them. Also the range of curvature values gradually decreases with time under the action of the surface diffusion process. It is worth mentioning that at time $t = 0.006t_b$ the pore surface profile changes from concave ($k < 0$) to convex and back to concave as one moves away from the tip (C or D) along the pore surface. A close-up of the pore surface profile near the boundary of the interparticle contact area (tip points C and D) at the very early stages of densification ($t = 0.00015t_b$ and $t = 0.01t_b$) is shown in Fig. 8. As has already been discussed, while almost the entire pore surface S_p' away from the tips is concave (see Fig. 7), there exist regions near the tips at the very early stages of the densification where the curvature reverses sign. The top inset in Fig. 8 shows a photograph of a sintered array of Cu wires reproduced from Alexander and Balluffi (1957), showing pores with both concavely and

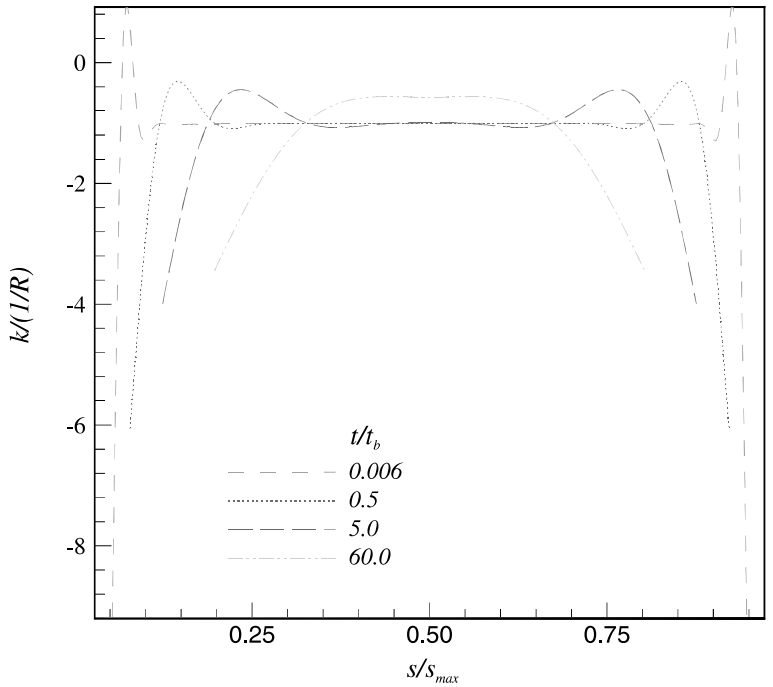

Fig. 7. Variation of pore surface curvature when surface diffusion is slow: $\chi_b = 5000$, $\chi_p = 20$, $\psi_p = 0.01$, $\psi_b = 0.003$, $\sigma_a/E = 0.001$, $n = 5$, and $v = 0.33$.

convexly curved regions. Thus, the present method qualitatively captures experimentally observed features at the microscale. As also seen from Fig. 7, finite element calculations at later stages ($t > 0.01t_b$) show no such curvature reversal and that the pore surface is always concave ($k < 0$). No curvature reversal occurred at any time in calculations with extremely fast pore surface diffusion (e.g., $\chi_p = 10^8$) and the pore surface was uniformly concave over the entire surface.

The relative density D of the powder compact was calculated by determining the area fraction occupied by the particles. The calculated evolution of relative density with time is shown in Fig. 9 for $\chi_p = 20$, 1000, and 10^8 while all other parameters were held fixed. As expected, greater densities are achieved for the same elapsed time when the surface diffusion is faster.

5.1. Comparison with other models

Hsueh and Evans (1981) and Riedel (1990) studied the compaction of hexagonal arrays of wires (2-D model) deforming by interparticle diffusion alone under the assumption of equilibrium-shaped pores and *plane strain conditions*. The corresponding predictions of densification rate are expressed by Eq. (17) in Hsueh and Evans (1981) and Eq. (2) in Riedel (1990). Svoboda and Riedel (1995) extended the work of Riedel (1990) to include the effect of coupled surface and interparticle diffusion, and derived an analytical approximation for the case of a pore with equilibrium shape given by their Eq. (23).

The densification rates predicted by the present model were calculated numerically from the D vs. t data (Fig. 9). These results along with those of Hsueh and Evans (1981), Riedel (1990), and Svoboda and Riedel (1995) are summarized in Fig. 10. As seen from Fig. 10, the Svoboda–Riedel model yields virtually the same

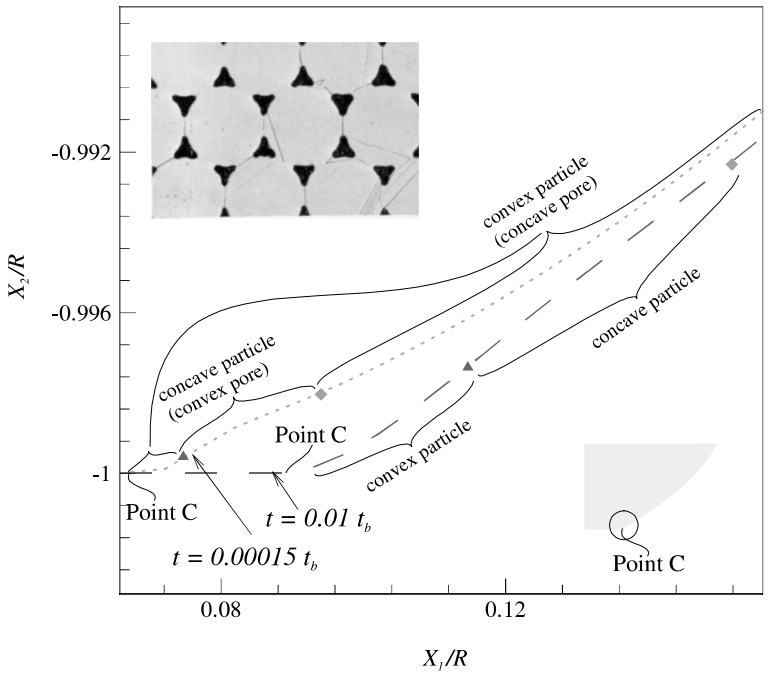

Fig. 8. Magnified view of pore profile near the tip when surface diffusion is slow ($\chi_p = 20$). Top inset shows experimentally observed curvature reversal in Cu wires (reprinted from *Acta Metallurgica* 5 (11), B.H. Alexander and R.W. Balluffi, 'The mechanism of sintering of copper', 666–677, copyright 1957, with permission from Elsevier Science) and the bottom inset shows the region that has been magnified.

densification rates for the three values of χ_p for the range of densities studied, indicating that it has a very weak dependence on surface diffusivity for the model parameters used.

The present investigation yields densification rates that are initially greater than those of the interparticle diffusion models, but rapidly decreasing as D increases. The very high densification rates during the early stages (low relative density) in the present investigation result from the rapid interparticle diffusion set up by the severe initial stress gradients. Those gradients are smaller in the Svoboda–Riedel model (see Fig. 11) since the contact size between the particles predicted by the Svoboda–Riedel model is greater than the calculated in the present investigation at a given relative density D and applied load σ_a. It is emphasized that the contact size in the present study is calculated as part of the solution to the entire initial-boundary value problem, whereas in the Svoboda–Riedel model the contact zone is calculated exclusively from the relative density and the dihedral angle (see their Eq. (15)). Also note that the uniform curvature of the assumed equilibrium shape for the pore in the Svoboda–Riedel model does affect the geometric calculation of the relative density, whereas in the present calculation there is no predetermined relationship between the curvature and the relative density.

As densification proceeds and the diffusional relaxation mechanisms tend to both weaken and neutralize these gradients (Fig. 11), the diffusion processes decelerate (see Figs. 5 and 6) and the densification rates drop to lower levels. The results of Fig. 10 for the small range of calculated relative densities, $0.79 \leqslant D \leqslant 0.83$, seem to indicate that the predicted densification rates of the present study tend to approach those of boundary diffusion models at higher densities. Indeed the corresponding calculated values of the contact zone size in the present study also tend to those of the Svoboda–Riedel model as the density increases.

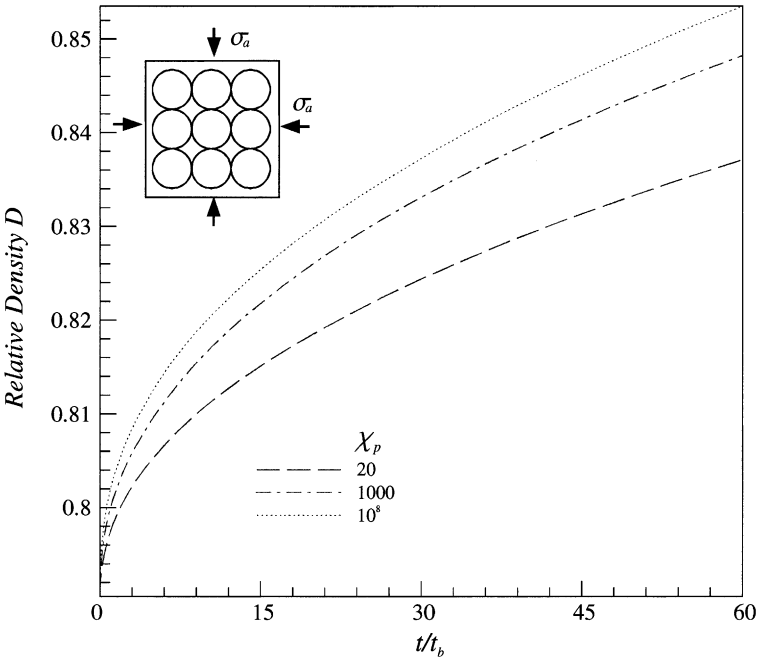

Fig. 9. Model predictions of relative density as a function of time: $\chi_b = 5000$, $\psi_p = 0.01$, $\psi_b = 0.003$, $\sigma_a/E = 0.001$, $n = 5$, and $v = 0.33$.

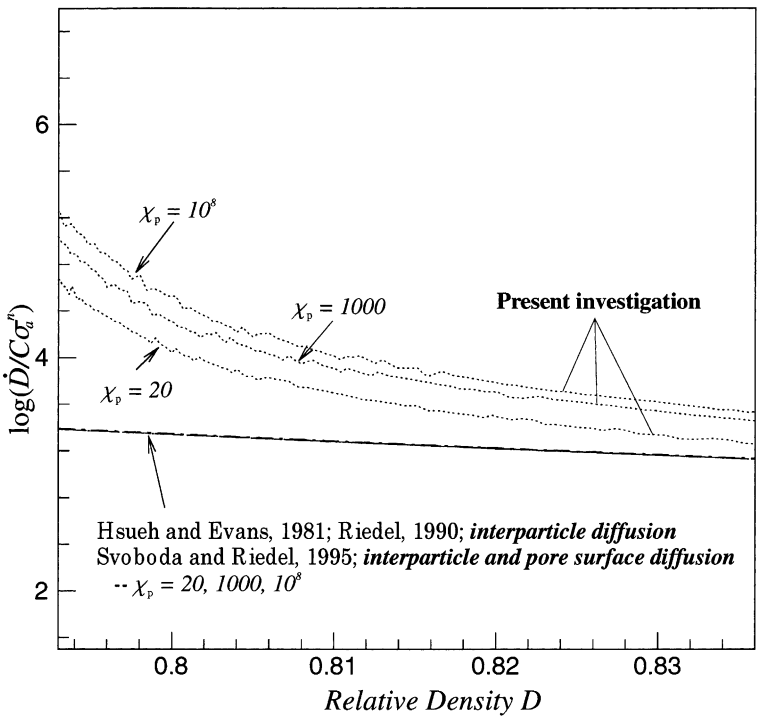

Fig. 10. Comparison of model predictions for plane-strain compaction.

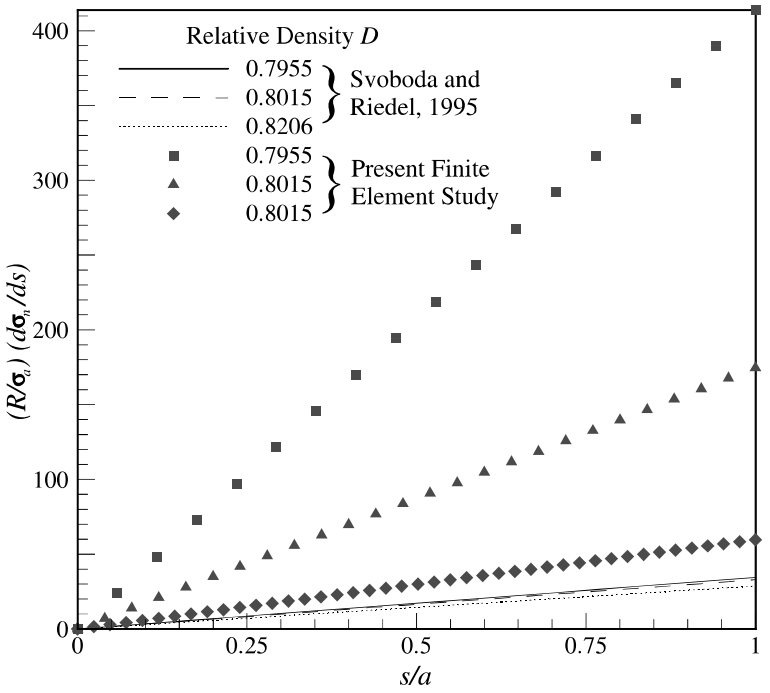

Fig. 11. Comparison of normal stress gradients on the interparticle contact area obtained from the present investigation with those predicted by the analytical model of Svoboda and Riedel (1995): $\chi_b = 5000$, $\chi_p = 20$, $\psi_p = 0.01$, $\psi_b = 0.003$, $\sigma_a/E = 0.001$, $n = 5$, and $v = 0.33$. Here s is arclength and a is the size of the contact zone.

6. Discussion

For a case of slow pore surface diffusion ($\chi_b = 5000,\ \chi_p = 20$), the pore curvature profile shows multiple extremum points during the early stages of densification (Fig. 7). Since the chemical potential is higher on the pore surface at regions of higher concavity ($k < 0$) and atoms there tend to move toward regions of convexity ($k > 0$) or less concavity, the flux profile changes sign at these extrema (Fig. 5). The surface diffusion process, though slow, does alleviate the curvature gradients and indeed, at the last time step shown in Fig. 7, there is only one peak value. On the other hand, in the case of extremely fast pore surface diffusion ($\chi_b = 5000,\ \chi_p = 10^8$) the curvature was found to be almost uniform over the entire pore surface with nearly negligible gradients. However, the extremely high value of the surface diffusion coefficient still ensures substantial mass flow (see Eq. (4)) over the pore (Fig. 6).

When the surface diffusion is fast ($\chi_b = 5000,\ \chi_p = 10^8$), the present calculations demonstrate that the particles deform as truncated cylinders since the pore surface was found to be of uniform concave curvature. On the other hand, Bouvard and McMeeking (1996) state, on the basis of their numerical studies, that even in the case of fast surface diffusion the particle surface in their axisymmetric model is not spherical. They drew this conclusion on the premise that $\xi = \mathscr{D}_b/\mathscr{D}_p = 0.02$ represented the fast pore surface diffusion limit in their calculations. Notice that the parameter ξ of Bouvard and McMeeking can be rewritten in terms of the dimensionless groups of the present study as $\xi = \chi_b\psi_p a_0^2/\chi_p R^2$. Taking into account that $\psi_p = 0.01$, one finds that the Bouvard and McMeeking fast surface diffusion limit corresponds to a χ_b/χ_p value of 1000 in the present investigation. Clearly, Fig. 5 indicates that even a χ_b/χ_p value of 250, which depicts pore surface diffusion faster than the fast pore surface diffusion limit of Bouvard and

McMeeking, actually corresponds to *slow* pore surface diffusion since mass transport away from the tips is not substantial. Hence, it appears that the calculations of Bouvard and McMeeking at $\xi = 0.02$ do not describe densification occurring at the fast surface diffusion limit, since those, according to the present study, would correspond to $\xi = 10^{-9}$. Of course, the Bouvard and McMeeking conclusion on the particle shape is correct at slow surface diffusion as the present study affirms (Figs. 4 and 8).

Certain models (e.g., Mullins, 1993; Riedel et al., 1994b; Zhang and Schneibel, 1995; Bouvard and McMeeking, 1996) for sintering provide solutions for the pore shape based on the important assumption that the equilibrium value for the dihedral angle, $\phi_{eq} = \arccos(\gamma_b/2\gamma_p)$, is always maintained at the tip. However, the angle at the tip equals ϕ_{eq} only when thermodynamic equilibrium is attained. In the case of sintering in the absence of external loads with no bulk deformation effects, which is the case considered by the classical models, thermodynamic equilibrium is indeed attained and the tip angle is dynamically maintained at its equilibrium value when surface diffusion is slow, as indicated by experiments by Wong and Pask (1979). On the other hand, in the case of pressure-assisted densification of particles that deform by means of mechanisms such as elasticity and power-law creep, there is no guarantee that the system achieves thermodynamic equilibrium as long as loading is maintained. In fact even in the case of pressureless sintering, when surface diffusion is fast the dihedral angle changes continuously with deformation as demonstrated in the experiments of Wong and Pask (1979) and discussed by Hoge and Pask (1977). Furthermore, the equilibrium angle in classical theory derives from a balance of grain boundary and surface tension (Herring, 1951) at the tip, and it does not account for energy associated with the adjacent elastically deforming material. In the present model, the customary local energy balance at the tip from which the equilibrium dihedral angle is calculated forms a part of the overall virtual power equation (algebraic terms of Eq. (12)). Thus, the present model makes no assumptions regarding the dihedral angle at the tip, thus accounting for a more general situation. Lastly, it is worth mentioning that several of the models in the literature do not enforce the dihedral angle (e.g., Kuczynski, 1949; Ashby, 1974; Bross and Exner, 1979; Exner, 1987; McMeeking and Kuhn, 1992) whereas others strictly enforce it (e.g., Mullins, 1993; Riedel et al. 1994b; Zhang and Schneibel, 1995; Bouvard and McMeeking, 1996).

7. Closure

Densification of a powder aggregate is a complex physical phenomenon involving multiple mechanisms characterized by a large number of material and geometric parameters. In the present study, important dimensionless groups have been identified, leading to a dramatic reduction in the number of case calculations required to analyze the process.

A finite element scheme has been developed to study the densification of a particle aggregate based on the interaction between the mechanisms acting at the microscale. In view of the complexity of the governing equations, one may consider the devised numerical techniques as rather efficient in predicting the values of both microscopic and macroscopic parameters when pore and particle shape changes are small. For predictions pertaining to densification at high relative densities ($>0.85\%$), the present model needs to be modified to account for geometric non-linearities.

Details have been presented on the variation of volumetric flux on the interparticle contacts and pore surface, and the pore surface curvature. The effectiveness of the diffusion processes in neutralizing stress/curvature gradients has been demonstrated through model calculations. Available models based on a single operating mechanism have been shown to underestimate the densification rates during the initial stages of densification, and the present model has successfully captured the experimentally observed pore curvature reversal.

Acknowledgements

This work was supported by the Department of Energy under grant DEFGO2-96ER45439. The authors would like to thank Professor R.S. Averback for many helpful discussions on the physics of the densification process.

Appendix A. Finite element formulation and solution of the initial boundary value problem for the equilibrium of the particle (problem (i))

Under plane strain conditions, the interparticle contact areas are assumed to be the two plane segments BC ($X_2 = -R$) and DE ($X_1 = R$) of Fig. 2. Arclength s is measured starting from point B and increases toward point E. The normal $\mathbf{n}$ is defined on the contact areas as positive when it points inwards as shown in Fig. 1a. A non-negative scalar gap function $\Delta g(s)$ at any point of the pore surface is defined to be its normal distance from the contact plane. Due to symmetry ($v^{\mathrm{II}} = 0,\ v^{\mathrm{I}} = v$), Eq. (6) is written as $\dot{h} = v_\alpha n_\alpha + \dot{g}$, $\alpha = 1$, 2 denoting vector components, and Eq. (5) as

$$\frac{\mathrm{d}j_{\mathrm{b}}}{\mathrm{d}s} + v_\alpha n_\alpha + \dot{g} = 0. \tag{A.1}$$

Following Needleman and Rice (1980) and employing piecewise linear functions to interpolate the velocities on each contact area, and applying the boundary conditions $j_{\mathrm{b}}(s_{\mathrm{B}}) = j_{\mathrm{b}}(s_{\mathrm{E}}) = 0$, one can integrate and cast Eq. (A.1) in finite element form as:

$$j_{\mathrm{b}}(s) = \{M(s)\}^{\mathrm{T}}\{v^{\mathrm{N}}\} - G(s), \tag{A.2}$$

where $\{M(s)\}$ is an array whose entries are the integrals of the linear interpolation functions used for the velocities (Needleman and Rice, 1980; Sofronis and McMeeking, 1994), $\{v^{\mathrm{N}}\}$ is the array of nodal velocities along the contact area, and $G(s)$ is a function of the gaps over the contact area (Subramanian and Sofronis, 1999).

If Δs is an infinitesimal segment of S_{p} subjected to an infinitesimal virtual normal displacement δu_{n}, then, it can be readily shown that $k\,\delta u_{\mathrm{n}}\Delta s = \delta(\Delta s)$. Thus, in finite element notation,

$$\int_{S_{\mathrm{p}}} \gamma_{\mathrm{p}} k\,\delta v_{\mathrm{n}}\,\mathrm{d}s = \int_{S_{\mathrm{p}}} \gamma_{\mathrm{p}}\,\delta\,\mathrm{d}\dot{s} = \sum_{i=1}^{N_{\mathrm{p}}-1} \gamma_{\mathrm{p}}\,\delta\dot{\ell}_i,$$

where N_{p} is the number of nodes on S_{p} and l_i is the length of the segment connecting nodes i and $i+1$. With the help of simple geometric analysis, one obtains $\delta\dot{\ell}_i = \{\delta v^{\mathrm{N}}\}^{\mathrm{T}}\{P_i\}$, where $\{P_i\}$ is a function only of the geometry of the pore at nodes i and $i+1$, and $\{\delta v^{\mathrm{N}}\}^{\mathrm{T}} = \left[\delta v_1^i, \delta v_2^i, \delta v_1^{i+1}, \delta v_2^{i+1}\right]$. Therefore,

$$\int_{S_{\mathrm{p}}} \gamma_{\mathrm{p}} k\,\delta v_{\mathrm{n}}\,\mathrm{d}s = \gamma_{\mathrm{p}} \sum_{i=1}^{N_{\mathrm{p}}-1} \{\delta v^{\mathrm{N}}\}^{\mathrm{T}}\{P_i\}. \tag{A.3}$$

Similarly, the algebraic terms of Eq. (12) are written as

$$\{\delta v^{\mathrm{N}}\}^{\mathrm{T}}\{F_\gamma\}, \tag{A.4}$$

where $\{F_\gamma\}$ is a function of γ_{b}, γ_{p}, and the tip angles at C and D; and $\{\delta v^{\mathrm{N}}\}^{\mathrm{T}} = \left[\delta v_1^{\mathrm{B}}, \delta v_1^{\mathrm{C}}, \delta v_2^{\mathrm{D}}, \delta v_2^{\mathrm{E}}\right]$.

Setting $\{v^{\mathrm{N}}\} = \{\Delta u^{\mathrm{N}}\}/\Delta t$, employing the standard interpolation matrices $[A]$ for the velocity and $[B]$ for the strain-rate inside the particle A, and substituting Eqs. (A.2), (A.3), and (A.4) into the governing Eq. (12), yields the non-linear finite element equations

$$\int_{\mathrm{A}} [B]^{\mathrm{T}}\{\sigma\}\,\mathrm{d}A + \left(\frac{1}{\mathscr{D}_{\mathrm{b}}\Delta t}\int_{S_{\mathrm{b}}} \{M(s)\}\{M(s)\}^{\mathrm{T}}\,\mathrm{d}s\right)\{\Delta u^{\mathrm{N}}\} = \{F\}, \tag{A.5}$$

where $\{F\}$ is the force vector given by

$$\{F\} = \frac{1}{\mathscr{D}_{\mathrm{b}}}\int_{S_{\mathrm{b}}} G(s)\{M(s)\}^{\mathrm{T}}\mathrm{d}s + \int_{S_T} [A]^{\mathrm{T}}\{T\}\,\mathrm{d}s - \sum_{i=1}^{N_{\mathrm{p}}-1}\gamma_{\mathrm{p}}\{P_i\} - \{F_\gamma\} - (\sigma_0)_{\mathrm{D}}\{M(s_{\mathrm{D}})\} + (\sigma_0)_{\mathrm{C}}\{M(s_{\mathrm{C}})\}. \tag{A.6}$$

The set of equations (A.5) is solved using a Newton iteration scheme, details of which can be found in Subramanian and Sofronis (1999).

Appendix B. Calculation of expansion α of the pore surface S_{p} (problem (ii))

Expansions $\{\alpha\}_{\mathrm{n}}$ at time t_{n} are known as well as the volumetric flux j_{C} and j_{D} at time t_{n+1} respectively at $s = s_{\mathrm{C}}$ and $s = s_{\mathrm{D}}$ (see Fig. 2) and the coordinates $\{X\}_{n+1} = \{X\}_{\mathrm{n}} + \{\Delta u\}$ of the nodes on the pore surface S_{p} from the solution to problem (i). The solution for the expansions $\{\alpha\}_{n+1}$ at time t_{n+1} is sought such that $\{\alpha\}_{n+1} = \{\alpha\}_{\mathrm{n}} + \{\Delta\alpha\}$.

Backward Euler integration of the mass conservation Eq. (7) yields

$$j_{\mathrm{p}}(s)\Delta t = j_{\mathrm{C}}\Delta t - \int_{s_{\mathrm{C}}}^{s} \Delta\alpha(s')\,\mathrm{d}s'. \tag{B.1}$$

Linear shape functions $\phi_i(s)$ are used to interpolate the expansion increments as $\Delta\alpha(s) = \sum_{i=1}^{N_{\mathrm{p}}}\phi_i(s)\Delta\alpha_i$ where $\Delta\alpha_i$ are the nodal expansion increments, and N_{p} is the total number of nodes along S_{p}. Thus, Eq. (B.1) is recast as

$$j_{\mathrm{p}}(s)\Delta t = j_{\mathrm{C}}\Delta t - \sum_{i=1}^{N_{\mathrm{p}}} m_i(s)\Delta\alpha_i, \tag{B.2}$$

which at $s = s_{\mathrm{D}}$ yields

$$j_{\mathrm{D}}\Delta t = j_{\mathrm{C}}\Delta t - \sum_{i=1}^{N_{\mathrm{p}}} m_i(s_{\mathrm{D}})\Delta\alpha_i. \tag{B.3}$$

The curvature k_i at nodal position i at time t_{n+1} is expressed as $k_i = k_i(\xi_r^{i-1}, \xi_r^i, \xi_r^{i+1})$, where

$$\xi_r^i = \left(X_r^i\right)_{\mathrm{n}} + \Delta u_r^i - (\alpha_i)_{n+1}n_r^i = \left(X_r^i\right)_{n+1} - (\alpha_i)_{\mathrm{n}}n_r^i - \Delta\alpha_i n_r^i = \bar{\xi}_r^i - \Delta\alpha_i n_r^i, \tag{B.4}$$

$r = 1, 2$ stands for components, $\bar{\xi}_r^i$ are known, and no summation is implied over the repeated index i. A linear approximation of k_i about the known value $\bar{k}_i = k_i\left(\bar{\xi}_r^{i-1}, \bar{\xi}_r^i, \bar{\xi}_r^{i+1}\right)$ yields

$$k_i = \bar{k}_i + \sum_{l=i-1}^{i+1}\left.\frac{\partial k_i}{\partial\alpha_l}\right|_{n+1}\Delta\alpha_l \tag{B.5}$$

and approximation of $\mathrm{d}k/\mathrm{d}s$ at the midpoint between nodes i and $i+1$ by a difference scheme as $\Delta k/\Delta s = (k_{i+1} - k_i)/(s_{i+1} - s_i)$ furnishes

$$\frac{\Delta k}{\Delta s} = \frac{1}{\Delta s}\left(\Delta\bar{k} + \sum_{l=i}^{i+2}\left.\frac{\partial k_{i+1}}{\partial\alpha_l}\right|_{n+1}\Delta\alpha_l - \sum_{l=i-1}^{i+1}\left.\frac{\partial k_i}{\partial\alpha_l}\right|_{n+1}\Delta\alpha_l\right) \tag{B.6}$$

Substituting Eq. (B.6) into Eq. (4) and combining it with Eq. (B.2), yields

$$j_{\mathrm{p}}\left(\frac{s_{i+1}+s_i}{2}\right)\Delta t = j_{\mathrm{C}}\Delta t - \sum_{i=1}^{N_{\mathrm{p}}} m_i\left(\frac{s_{i+1}+s_i}{2}\right)\Delta\alpha_i$$
$$= \frac{\gamma_{\mathrm{p}}\mathscr{D}_{\mathrm{p}}}{\Delta s}\left(\Delta\bar{k} + \sum_{l=i}^{i+2}\left.\frac{\partial k_{i+1}}{\partial\alpha_l}\right|_{n+1}\Delta\alpha_l - \sum_{l=i-1}^{i+1}\left.\frac{\partial k_i}{\partial\alpha_l}\right|_{n+1}\Delta\alpha_l\right). \tag{B.7}$$

Equation (B.7) represent the enforcement of Eqs. (4) and (7) at the midpoints of the segments between the N_{p} pore surface nodes. These $N_{\mathrm{p}}-1$ equations combined with Eq. (B.3) yield a system of N_{p} equations for the N_{p} unknown values of $\Delta\alpha_i$. This system was solved under the constraint that the symmetry of the unit cell be maintained.

References

Akisanya, A.R., Cocks, C.F., 1995. Stage I compaction of cylindrical particles under non-hydrostatic loading. J. Mech. Phys. Solids 43 (4), 605–636.

Akisanya, A.R., Cocks, A.C.F., Fleck, N.A., 1994. Hydrostatic compaction of cylindrical particles. J. Mech. Phys. Solids 42 (7), 1067–1085.

Alexander, B.H., Balluffi, R.W., 1957. The mechanism of sintering of copper. Acta Metal. 5 (11), 666–677.

Arzt, E., 1982. The influence of an increasing particle coordination on the densification of spherical powders. Acta Metal. 30 (10), 1883–1890.

Arzt, E., Ashby, M.F., Easterling, K.E., 1983. Practical applications of hot-isostatic pressing diagrams: Four case studies. Metall. Trans. A 14A (2), 211–221.

Ashby, M.F., 1974. A first report on sintering diagrams. Acta Metal. 22 (3), 275–289.

Bouvard, D., 1993. Modeling the densification of powder composites by power law creep. Acta Metal. Mater. 41 (5), 1413–1420.

Bouvard, D., McMeeking, R.M., 1996. The deformation of interparticle necks by diffusion controlled creep. J. Am. Ceram. Soc. 79 (3), 666–672.

Bross, P., Exner, H.E., 1979. Computer simulation of sintering processes. Acta Metal. 27 (6), 1013–1020.

Casagranda, A., Sofronis, P., 1997. Numerical observations of scaling laws in the consolidation of powder compacts. Acta Mater. 45 (11), 4835–4845.

Chuang, T.-Z., Kagawa, I.K., Rice, J.R., Sills, L.B., 1979. Non-equilibrium models for diffusive cavitation of grain interfaces. Acta Metal. 27 (3), 265–284.

Cocks, A.C.F., 1989. Inelastic deformation of porous materials. J. Mech. Phys. Solids 37 (6), 693–715.

Cocks, A.C.F., 1994. The structure of constitutive laws for the sintering of fine-grained materials. Acta Metal. Mater. 42 (7), 2191–2210.

Duva, J., Crow, P.D., 1992. The densification of powders by power law creep during hot isostatic pressing. Acta Metal. Mater. 40 (1), 31–35.

Exner, H.E., 1987. Neck shape and limiting GBD/SD ratios in solid state sintering. Acta Metal. 35 (3), 587–591.

Fishcmeister, H.F., Arzt, E., 1983. Densification of powders by particle deformation. Pow. Metal. 26 (2), 82–88.

Fleck, N.A., 1995. On the cold compaction of powders. J. Mech. Phys. Solids 43 (9), 1409–1431.

Fleck, N.A., Kuhn, L.T., McMeeking, R.M., 1992. Yielding of metal powder bonded by isolated contacts. J. Mech. Phys. Solids 40 (5), 1139–1162.

Freund, L.B., Beltz, G.E., Jonsdottir, F., 1993. Continuum modeling of stress-driven surface diffusion in strained elastic materials. Mat. Res. Soc. Symp. Proc. 308, 383–394.

Gurtin, M.E., Murdoch, A.I., 1975. A continuum theory of elastic material surfaces. Arch. Rat. Mech. Anal. 57 (4), 291–323.

Helle, A.S., Easterling, K.E., Ashby, M.F., 1985. Hot-isostatic pressing diagrams: new developments. Acta Metal. 33 (12), 2163–2174.

Herring, C., 1951. Surface tension as a motivation for sintering. In: The Physics of Powder Metallurgy – A symposium held at Bayside, LI, New York, 24–26 August, 1949, pp. 143–179.

Hoge, C.E., Pask, J.A., 1977. Thermodynamic and geometric considerations of solid state sintering. Ceramurgia Int. 3 (3), 95–99.

Hsueh, C.H., Evans, A.G., 1981. Creep Fracture in Ceramic Polycrystals – II. Effects of inhomogeneity on creep rupture. Acta Metal. 29 (12), 1907–1917.

Kuczynski, G.C., 1949. Self-diffusion in sintering of metallic particles. Trans. AIME 185, 169–177.

Kuhn, L.T., McMeeking, R.M., 1992. Power law creep of powder bonded by isolated contacts. Int. J. Mech. Sci. 34 (7), 563–573.

Larsson, P.-L., Biwa, S., Storakers, B., 1996. Analysis of cold and hot isostatic compaction of spherical particles. Acta Mater. 44 (9), 3655–3666.

McMeeking, R.M., Kuhn, L.T., 1992. A diffusional creep law for powder compacts. Acta Metal. Mater. 40 (5), 961–969.

Mullins, W.W., 1993. Idealized two dimensional sintering by interface diffusion. Scripta Met. Mater. 29 (4), 491–496.

Nagtegaal, J.C., Parks, D.M., Rice, J.R., 1974. On numerically accurate finite element solutions in the fully plastic range. Comp. Meth. Appl. Mech. Engng. 4 (2), 153–177.

Needleman, A., Rice, J.R., 1980. Plastic creep flow effects in the diffusive cavitation of grain boundaries. Acta Metal. 28 (10), 1315–1332.

Pan, J., Cocks, A.C.F., 1995. A numerical technique for the analysis of coupled surface and grain-boundary diffusion. Acta Metal. Mater. 43 (4), 1395–1406.

Raj, R., 1974. Transient behavior of diffusion-induced creep and creep rupture. Metall Trans. A. 6A (8), 1499–1509.

Pan, J., Cocks, A.C.F., Kucherenko, S., 1997. Finite element formulation of coupled grain-boundary and surface diffusion with grain-boundary migration. Proc. Roy. Soc. Lond. A 453, 2161–2184.

Rice, J.R., Chuang, T.-J., 1981. Energy variations in diffusive cavity growth. J. Am. Ceram. Soc. 64 (1), 46–53.

Riedel, H., 1990. A constitutive model for the finite-element simulation of sintering – distortions and stresses. In: Messing, G.L., Hirano, S.-I., Hausner, H. (Eds.), Ceramic Transactions, Ceramic Powder Science III, vol. 12. Westerville, Ohio, pp. 619–630.

Riedel, H., Kozak, V., Svoboda, J., 1994a. Densification and creep in the final stage of sintering. Acta Metal. Mater. 42 (9), 3093–3103.

Riedel, H., Zipse, H., Svoboda, J., 1994b. Equilibrium pore surfaces, sintering stresses and constitutive equations for the intermediate and late stages of sintering – II. Diffusional densification and creep. Acta Metal. Mater. 42 (2), 445–452.

Sofronis, P., McMeeking, R.M., 1992. Creep of power-law material containing spherical voids. J. Appl. Mech. 59 (2), 88–95.

Sofronis, P., McMeeking, R.M., 1994. The effect of interface diffusion and slip on the creep resistance of particulate composite materials. Mech. Mater. 18 (2), 55–68.

Storakers, B., Biwa, S., Larsson, P.-L., 1997. Similarity analysis of inelastic contact. Int. J. Solid Struct. 34 (24), 3061–3083.

Storakers, B., Fleck, N.A., McMeeking, R.M., 1999. The viscoplastic compaction of composite powders. J. Mech. Phys. Solids 47 (4), 785–815.

Storakers, B., 1997. Local contact behaviour of viscoplastic particles. In: Fleck, N.A., Cocks, A.C.F. (Eds.), IUTAM Symposium on Mechanics of Granular Flow and Powder Compaction, 15–17 July, 1996, Cambridge, UK, Kluwer Academic Publishers, pp. 173–184.

Subramanian, S.J., Sofronis, P., 1999. Modeling of the interaction between densification mechanisms in powder compaction. University of Illinois at Urbana-Champaign, TAM Report No. 907, May 1999.

Suo, Z., Wang, W., 1994. Diffusive void bifurcation in stressed solid. J. Appl. Phys. 76 (6), 3410–3421.

Svoboda, J., Riedel, H., 1995. Quasi-equilibrium sintering for coupled grain-boundary and surface diffusion. Acta Metal. Mater. 43 (2), 499–506.

Svoboda, J., Riedel, H., Zipse, H., 1994. Equilibrium pore surfaces, sintering stresses and constitutive equations for the intermediate and late stages of sintering – I. Computation of equilibrium surfaces. Acta Metal. Mater. 42 (2), 435–443.

Swinkels, F.B., Ashby, M.F., 1981. A second report on sintering diagrams. Acta Metal. 29 (2), 259–281.

Wang, W., Suo, Z., 1997. Shape change of a pore in a stressed solid via surface diffusion motivated by surface and elastic energy variation. J. Mech. Phys. Solids 45 (5), 709–729.

Wong, B., Pask, J.A., 1979. Experimental analysis of sintering of MgO compacts. J. Am. Ceram. Soc. 62 (3–4), 141–146.

Xia, L., Bower, A.F., Suo, Z., Shih, C.F., 1997. A finite element analysis of the motion and evolution of voids due to strain and electromigration induced surface diffusion. J. Mech. Phys. Solids 45 (9), 1473–1493.

Zhang, W., Schneibel, J.H., 1995. The sintering of two particles by surface and grain-boundary diffusion – a two-dimensional numerical study. Acta Metal. Mater. 43 (12), 4377–4386.